

## Auxiliary material

### 1. Compilation of GPS data-sets

#### 1.1. New GPS data in central Chile

Since 2007, the french-chilean central Chile network described in details by *Vigny et al.* [2009] was remeasured 4 times at 6 months intervals (May 2007, December 2007, May 2008 and December 2008). Thus, surveys cover the period ranging from May 2004 to December 2008. Several sites have been added over the years, but most of the 33 sites have been surveyed 10 times over this 4 year-period. All sites of this network but 2 are equipped with bolts sealed in bedrock outcrops that enable direct antenna centering with sub-millimeter accuracy. They were all measured using a single type of Ashtech ZXtreme dual-frequency receivers equipped with the same type of antennae (Ashtech Geodetic IV). During all campaigns, at least four cGPS sites (LVIL and SLMC in the south and OVLL and TOLO in the north) were included. All survey sites were measured for at least three 12 to 24 hours sessions (often more).

We publish here an update of this network interseismic velocities including 5 new sites. Data processing was done using exactly the same procedure as described in *Vigny et al.* [2009]. We use GAMIT software to reduce 24-h sessions to daily estimates of station positions, using the ionosphere free L3 observable and fixing ambiguities to integer values whenever possible. We estimate one tropospheric vertical delay parameter per station every 3 h.

---

In the second step, we combine the daily solutions using the GLOBK software [Herring, 2009]. To define a consistent reference frame for all epochs, we include tracking data from a selection of permanent stations (19) in South America, some of them belonging to the IGS. Seven stations are within or very close to the deformation area, 10 more span the South-American craton in Brazil, Guyana and Argentina, and the remaining two sample the Nazca plate. We combine daily solutions using Helmert-like transformations to estimate translation, rotation, scale and Earth orientation parameters (polar motion and UT1 rotation via GLORG software). This stabilization procedure defines a reference frame by minimizing (in the least-square sense) the departure from a-priori values, here given by the International Terrestrial Reference Frame (ITRF) 2005 [Altamimi et al., 2007]. This procedure estimates the positions and velocities for a set of ten well-determined stations in and around our study area (BRAZ, FORT, KOUR, LPGS, RIOG, SANT, CHPI, CONZ, ISPA, GLPS). The misfit to these stabilization stations is 0.41mm in position and 2.4 mm/yr in velocity. This procedure leads to horizontal and vertical velocities defined in the ITRF2005. Then, we compute velocities relative to the South-American plate by using the angular velocity of this plate ( $25.4^{\circ}\text{S}$ ,  $124.6^{\circ}\text{W}$ ,  $0.11^{\circ}/\text{Myr}$ ) given in the NNR-Nuvel-1A model [DeMets Gordon, 1994].

The new velocities published in table S1 differ from the previously published ones by no more than 1-2 millimeters per year on each components. Opposite to Vigny et al. [2009], we decided to publish also vertical velocities to which we assign a  $2\sigma$  uncertainty. To exclude noisy and incoherent velocities, we reject those that are determined with a normalized RMS higher than 1.7. This corresponds to average residuals greater than 3 times the average data uncertainties. We used the GLRED software and procedures to



estimate time-series for those vertical data. Time-series of four rejected and four accepted vertical velocities are plotted on Figure S1.

## 1.2. Horizontal velocities

In many previously published studies (see table S3) the usual strategy has been to publish the GPS data in a self-defined fixed South-America (SOAM) reference frame based on the minimization of the velocities of several fiducial stations located on the Brazilian and Argentine craton. The publication of the data in those unclear reference frames instead of in the ITRF, introduces a major difficulty in combining those studies. Because the self made SOAM reference frames are realized using permanent stations available at the time of the surveys, they are time-span dependent. Thus, even the reference frames defined by the same team for different data-sets and time spans are different. This highly complicates the comparison between published data-sets.

We decide to rotate the compiled data-set in the well known NNR-NUVEL1A South American fixed reference framed defined by the SOAM rotation pole ( $25.4^{\circ}\text{S}$ ,  $124.6^{\circ}\text{W}$ ,  $0.11^{\circ}/\text{Myr}$  [*DeMets Gordon, 1994*]). Data-sets published in this NNR-Nuvel1A reference frame [*Ruegg et al., 2009*] and [*this study*] are used as reference and we compute the difference between these and the other data-sets at common points. For each data-set, we invert for the rotation pole that minimizes the residuals at 4 fiducial stations at least, and apply it to the data (see details of the inversion and rotation in table S4). For the SAGA-Central-2 data-set [*Khazaradze and Klotz, 2003*], we lack common measurements at fiducial stations. We use the residuals between the LiA-MdB-Central [*this study*] and the SAGA-Central-2 velocities at four pairs of very close stations to invert for the rotation pole (i.e LCHU/AR90, ZAHU/AR70, PATI/CO50 and TOPI/TO10).

While most of the data-sets are compatible, this work underlies some inherent discrepancies between the SAGA data-set and the other data-sets : the SAGA velocity field is coherent with the other sets near the coast but not in the intermediate to far-field area where the SAGA velocities are systematically lower (up to  $\sim 5$  mm/yr in some places, see Figure 6). In other words, the gradient of deformation is larger in the SAGA set than in any other one. This observation could result either from the data processing, definition of the SOAM referential used in [Klotz *et al.*, 2001; Khazaradze and Klotz, 2003], scaling issues, or less probably from a tectonic behavior. We did not find any rigid rotation that enables the original data-set to become fully coherent with the other studies.

### 1.3. Vertical velocities

Vertical velocities are less precise and potentially more affected by seasonal effects than horizontal velocities. Therefore, most studies refrain from publishing campaign-mode vertical velocities, with the notable exception of Ruegg *et al.* [2009]. We use in this study a subset of those published velocities based on several quality criteria. A velocity must be based on more than 2-year time span measurements, its formal uncertainty have to be smaller than 5.5 mm/yr, and it must be coherent with nearby cGPS stations if available. This way, only six velocities were excluded from the original data set, and the final set is presented in table S2.

The vertical data extracted both from [Ruegg *et al.*, 2009] and [this study] are presented on Figure 4. Profiles at different latitudes in Central Chile underline major differences along the subduction strike. Finally, vertical displacements in the Concepción-Constitución area due to the Maule earthquake (February 27th 2010,  $M_w 8.8$ ), are opposite

and complementary to interseismic vertical velocities determined by *Ruegg et al.* [2009] (Figure 4).

We present in supplementary Figure S5 the coupling distribution obtained without including the vertical data in the inversion, and the fit of the predicted deformation to these vertical data on four profile lines. The interseismic coupling pattern is very similar to the one determined in our “best-model” presented in Figure 5-c (which uses the vertical data), and the fit to the horizontal data is good (hrms 1.2). This coupling distribution yields a good fit to the vertical data set, except in the Tongoy area where it underestimates the observed surrection. Thus, we are confident that those vertical velocities are fully coherent with the horizontal ones and impose few additional constrains on the inversion.

#### 1.4. Weighting of the data sets

In order to get for every data-set a RMS value close to their average uncertainty, we “scaled up” the CAP, SAGA and LiA-MdB-south data-set uncertainties. To do so, we multiply their published uncertainties by a scaling factor detailed in table S5. The formal uncertainties of *Ruegg et al.* [2009] vertical velocities were increased by a factor of 3. This leads to reasonable  $\chi^2$  values in our favorite model (close to 1).

## 2. Modelling strategy

### 2.1. Backslip hypothesis

During the interseismic phase of the seismic cycle, the convergent plate motion generates elastic deformation of the upper plate. *Okada* [1985] described this deformation as equivalent to the deformation pattern caused by a dislocation buried in a semi-infinite, elastic, homogeneous medium. Okada’s equations can be applied to the interseismic load-

ing phase using the “backslip” assumption [*Savage, 1983*]. This assumption claims that the deformation caused by the locked portion of the fault is equivalent to the addition of the deformation caused by the long-term convergence motion between both plates, and the deformation caused by a normal slip dislocation occurring on the coupled area. This last term is called the “backslip” component. This hypothesis has been extensively used to model upper plate deformation (e.g [*McCaffrey, 2002; Wallace et al., 2004; Socquet et al., 2006*]), and is often criticized because of a misinterpretation of the “long-term” steady state component that is sometimes considered as a dislocation-like component that causes discontinuities in the near-trench deformation field [*Vergne et al., 2001*]. However, *Kanda and Simons* [2010] recently showed that without this mislead interpretation of Savage’s steady-state component and even for curved fault geometries, the backslip assumption allows to simulate correctly the upper plate deformation.

To quantify the amount of coupling, we use the DEFNODE inversion program based on the backslip assumption [*McCaffrey, 2002*]. The long-term relative block motion on the subduction is fixed in our case by the relative pole between Nazca and South American plate determined by *Vigny et al.* [2009] (55.9°N, 95.2°W, 0.610 °/My). The subduction interface is discretized as a grid of nodes modelled as source points. Surface deformation generated by each of these nodes is described by individual Green’s functions that are summed to obtain the total interseismic deformation field. The coupling value for each node is inverted with a downhill simplex method to obtain the “best” coupling distribution fitting the GPS data-set, i.e the model that minimizes the reduced  $\chi_n^2$  function with

$$\chi_n^2 = \sum_{i=1,n} \left( \frac{r_i}{f\sigma_i} \right)^2 (n - P)^{-1} \quad (1)$$

where  $n$  is the number of observations (620 in our case),  $P$  the number of free parameters in the inversion (420 in our case),  $r_i$  is the residual value at a point,  $\sigma_i$  the formal data uncertainty and  $f$  a data scaling factor (table S5). The coupling coefficient  $\Phi$  is defined as :  $V_{\text{backslip dislocation}} = -\Phi.V_{\text{convergence}}$ , meaning that a 100% coupling coefficient implies a fully locked zone, whereas a less than 100% coupling coefficient is a partially coupled zone where the convergence is accommodated by both seismic rupture and creep.

## 2.2. Spatial resolution and constraints on the inversion

We estimate the resolution of our inversion with checkerboard tests, with or without random noise added to the synthetic data-set, and with or without roughness coefficient imposed (Figure S2). We have no resolution for the shallowest part of the interface (from 0 to 15 km depth) except in the La Serena area (30°S) where the distance between the coast and the trench is  $\sim 70$  km and allows for better insight of the shallow interface. We also conducted inversions forcing the shallow interface to be 100% coupled (Figure S3). In these tests, if the interface is locked down to 7 km depth or less (figures S3-1 and 2), the coupling distributions reproduce the data with good RMS (lower than 1.5) and depict the same lateral variations than in our favorite model. If the interface is locked down to 15 km or deeper (figures S3-3 and 4), the normalized RMS increases significantly and the residuals are pointing westward in a systematic way, notably in the La Serena area. This implies that in general we are not able to conclude whether the shallow interface (down to 15 km depth) is locked during the interseismic loading or is freely creeping. In the La Serena area (30°S), the vicinity between the trench and the coast (70 km locally) and the high density of our measurements increase the resolution up to  $\sim 10$  km depth. Deepest parts of the interface are homogeneously unresolved (more than 80 km depth).

As suggested by *McCaffrey* [2002] to avoid lateral effects, we impose a similar coupling value for the last two nodes at both fault ends and we fix the deepest line of nodes to a zero coupling value. We minimize the numerical instabilities by introducing an along strike roughness coefficient of  $0.7/^\circ$  for the surface nodes (i.e. the coupling value between nodes distant of 111 km is not allowed to differ by more than 0.7) which decreases in depth linearly towards a 0 roughness for the deepest nodes (120 km depth). We chose this roughness value as it yields the best compromise between smoothing and RMS (see insert in Figure S4), i.e highest roughness values don't yield significant improvement of the fit. Imposing this along strike and along dip smoothing leads to an overall underestimate of the amount of coupling due to the softening of sharp contrasts, but the general pattern is reasonably well retrieved (see Figure S2). Furthermore, the decrease of the roughness coefficient with depth does not allow for sharp lateral variations at depth greater than 60 km.

### 2.3. Alternative models

The physical meaning of a low coupled updip transition zone is still debated [*McCaffrey*, 2002; *Wang and Dixon*, 2004; *Lay and Schwartz*, 2004; *Wang and Dixon*, 2004]. This is mostly due to the fact that anywhere on Earth, the distance between the trench and the coast is too large (more than 70 km) and prevents us to have sufficient resolution to image the shallow interface (from surface to 15 km depth). Thus, several modelling strategies were used in previous studies : most of them fix the shallowest part of the interface to a coupling coefficient of 100%, whereas *McCaffrey* [2002] and *Wallace et al.* [2004] proposed to force the coupling coefficient to decrease with depth (“ddc” or down-dip decrease option implemented in DEFNODE). In this study, we chose to present in the main text a very

smoothed first-order model in which we used the down-dip decrease constraint, side by side with our favorite model in which neither the amplitude of the shallow coupling nor its downdip variation was constrained (Figure 5). Here, we present alternative models that reproduce reasonably the data set and that include a-priori constraints on the coupling of the shallow interface. Among those models, those which reproduce the data with a normalized RMS lower than 1.5 were used to characterize the latitudinal variations of the average coupling coefficient presented in Figure 8. All together, they show similar pattern and define the large scale variations of the coupling coefficient along Central Chile.

First, we conduct inversions in which coupling is artificially set to 100% for the shallowest nodes of the grid (Figure S3). When the shallow locked zone extent down to 7 km depth or less (Figure S3-1 and 2), the fit to the whole data set is good and the normalized RMS is lower than 1.5. The robust features of our favorite model are persistent in those models : the coupling distribution is again characterized by four segments and associated intersegments.

Second, we tested the effect of imposing a downdip decrease in coupling coefficient as suggested by *McCaffrey* [2002] and *Wallace et al.* [2004] in the inversion of the coupling distribution. We present several models obtained with this constraint using variable roughness values in the supplementary Figure S7. Those models fit the first order of the data set but fail in retrieving the coastal deformation in the Concepción-Constitución area and the whole deformation pattern of the San Antonio region ( $\sim 34^\circ$ ). Nevertheless, the general pattern in the coupling distribution is still persistent.

## References

- Altamimi Z., Collilieux X., Legrand J., Garayt B., and Boucher C. ITRF2005: A new release of the International Terrestrial Reference Frame based on time series of station positions and Earth Orientation Parameters. *J. Geophys. Res.*, 112(B9):B09401, 2007.
- Brooks B.A., Bevis M., Smalley R. Jr, Kendrick E., Manceda R., Lauría E., Maturana R., and Araujo M. Crustal motion in the Southern Andes (26–36 S): Do the Andes behave like a microplate? *Geochem. Geophys. Geosyst*, 4(10):1085, 2003.
- Bevis M., Kendrick E.C., Smalley R. Jr, Herring T., Godoy J., and Galban F. Crustal motion north and south of the Arica deflection: comparing recent geodetic results from the Central Andes. *Geochem. Geophys. Geosyst*, 1(12):1005, 1999.
- DeMets Gordon R. Effect of recent revisions to the geomagnetic reversal timescale on estimates of current plate motions, *Geophys. Res. Lett*, 2(20):2191–2194, 1994.
- Herring TA. Documentation of the GLOBK software version 10.35. *Mass. Inst. of Technol., Cambridge*, 2009.
- Kanda R.V.S. and Simons M. An elastic plate model for interseismic deformation in subduction zones. *J. Geophys. Res.*, 115(B3):B03405, 2010.
- Khazaradze G. and Klotz J. Short-and long-term effects of GPS measured crustal deformation rates along the south central Andes. *J. Geophys. Res.*, 108(B6):2289, 2003.
- Klotz J., Khazaradze G., Angermann D., Reigber C., Perdomo R., and Cifuentes O. Earthquake cycle dominates contemporary crustal deformation in Central and Southern Andes. *Earth Planet. Sci. Lett.*, 193(3-4):437–446, 2001.
- Lay T. and Schwartz S. Comment on Coupling semantics and science in earthquake research,. *Eos Trans. AGU*, 85(36):339–340, 2004.



- McCaffrey R. Crustal block rotations and plate coupling. *Plate Boundary Zones, Geodyn. Ser.*, 30:101–122,
- Moreno MS, Klotz J., Melnick D., Echtler H., and Bataille K. Active faulting and heterogeneous deformation across a megathrust segment boundary from GPS data, south central Chile (36–39 S). *Geochem. Geophys. Geosyst.*, 9:36–39, 2008.
- Okada Y. Surface deformation due to shear and tensile faults in a half-space. *Bull. Seismol. Soc. Amer.*, 75(4):1135–1154, 1985.
- Ruegg JC, Rudloff A., Vigny C., Madariaga R., De Chabalier JB, Campos J., Kausel E., Barrientos S., and Dimitrov D. Interseismic strain accumulation measured by GPS in the seismic gap between Constitución and Concepción in Chile. *Phys. Earth Planet. Inter.*, 175(1-2):78–85, 2009.
- Savage JC. A dislocation model of strain accumulation and release at a subduction zone. *J. Geophys. Res.*, 88(B6), 1983.
- Socquet A., Simons W., Vigny C., McCaffrey R., Subarya C., Sarsito D., Ambrosius B., and Spakman W. Microblock rotations and fault coupling in SE Asia triple junction (Sulawesi, Indonesia) from GPS and earthquake slip vector data. *J. Geophys. Res.*, 111 (B8):B08409, 2006.
- Vergne J., Cattin R., and Avouac JP. On the use of dislocations to model interseismic strain and stress build-up at intracontinental thrust faults. *Geophys. J. Int.*, 147(1): 155–162, 2001.
- Vigny C., Rudloff A., Ruegg J.C., Madariaga R., Campos J., and Alvarez M. Upper plate deformation measured by GPS in the Coquimbo Gap, Chile. *Phys. Earth Planet. Inter.*, 175(1-2):86–95, 2009.

Wallace L.M., Beavan J., McCaffrey R., and Darby D. Subduction zone coupling and tectonic block rotations in the North Island, New Zealand. *J. Geophys. Res.*, 109(B12): B12406, 2004.

Wang K. and Dixon T. “Coupling” Semantics and Science in Earthquake Research. *EOS Trans. AGU*, 85:180, 2004.

Wang K. and Dixon T. Reply [to “Comment on Coupling semantics and science in earthquake research”]. *EOS Trans. AGU*, 85:340, 2004.

Reliable velocities

Excluded velocities

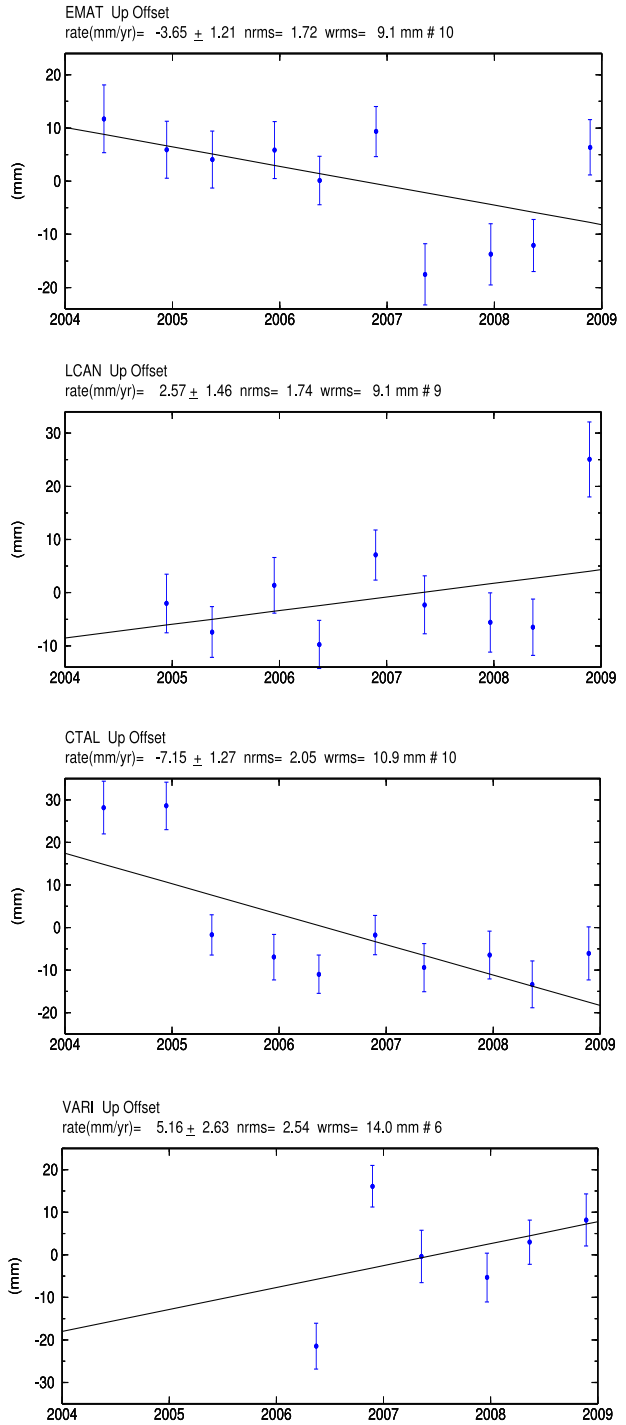
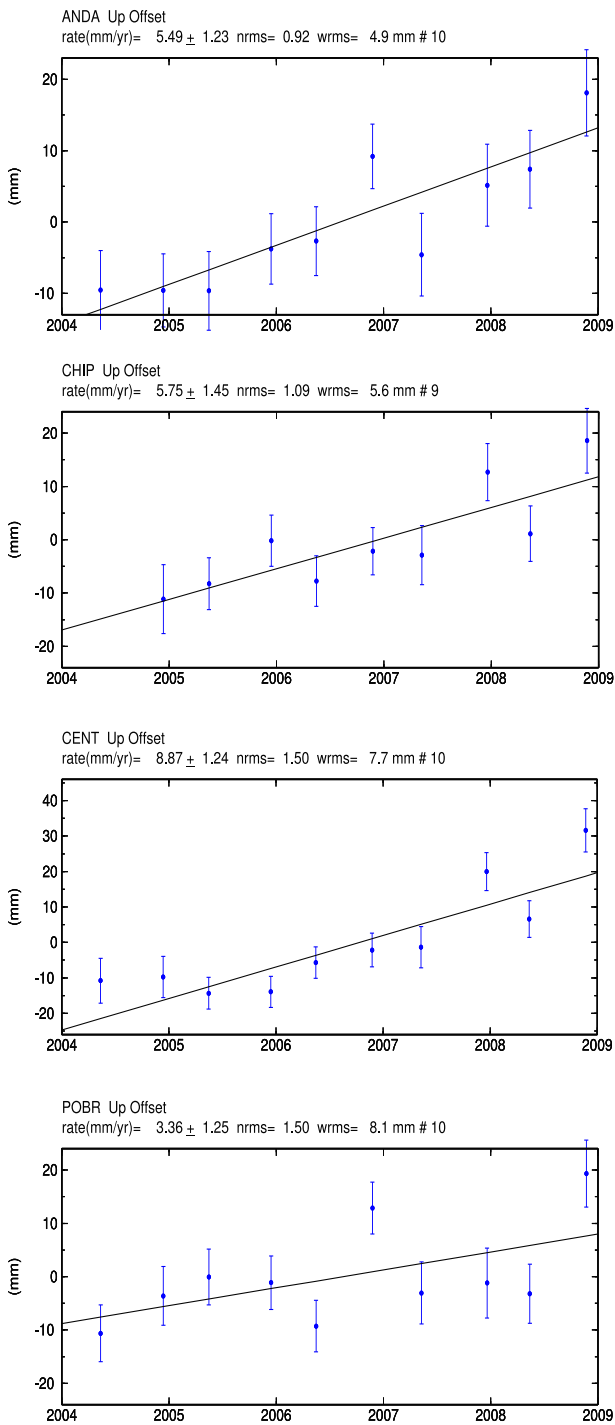


**Figure S1.** Subset of vertical time series of measurement points of the LiA-central network considered as reliable (left) or not (right). Stations on the right are excluded because the normalized rms of the time-series are greater than 1.7.

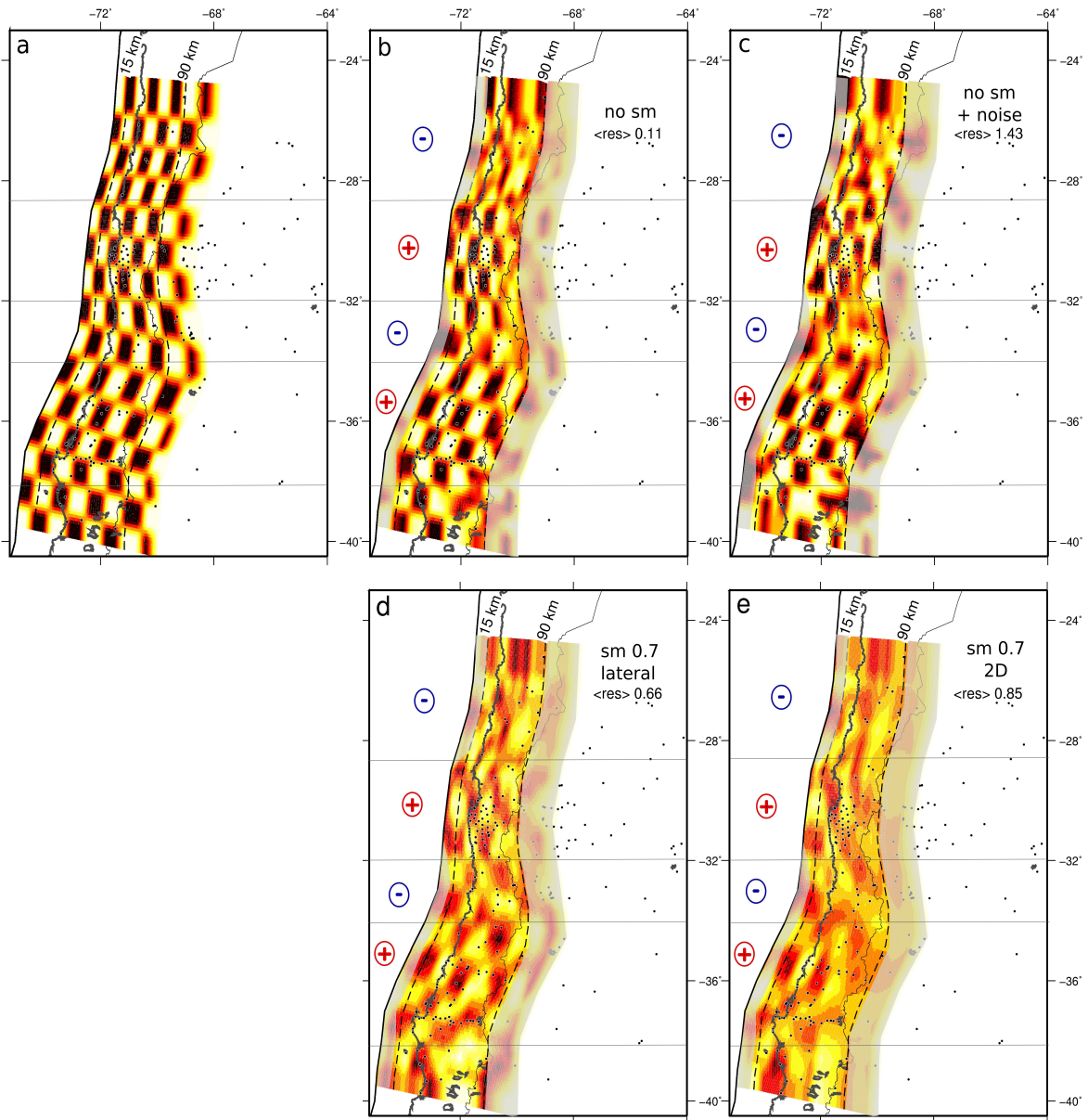


**Figure S2.** Checkerboard resolution tests. (a) Synthetic checkerboard coupling distribution of 100% (red patches) and 0% (light yellow patches) coupled asperities for our favorite geometry. (b) Inverted coupling distribution obtained using the raw synthetic surface deformation field generated by the checkerboard, without roughness coefficient. (c) Retrieved coupling when random noise is added to the synthetic surface deformation field, without roughness coefficient. (d) and (e), inverted coupling distribution obtained using the raw synthetic surface deformation field, and imposing a 0.7 roughness coefficient that is either constant or decreasing along dip, respectively. Dashed lines are the slab isodepth. Black circles are the measurement points. The average residual in mm/yr is indicated on the upper right corner except for (a). Well or poorly resolved area are indicated with plus or minus symbols respectively. Grey shaded areas mask the very shallow or very deep unresolved parts of the slab.

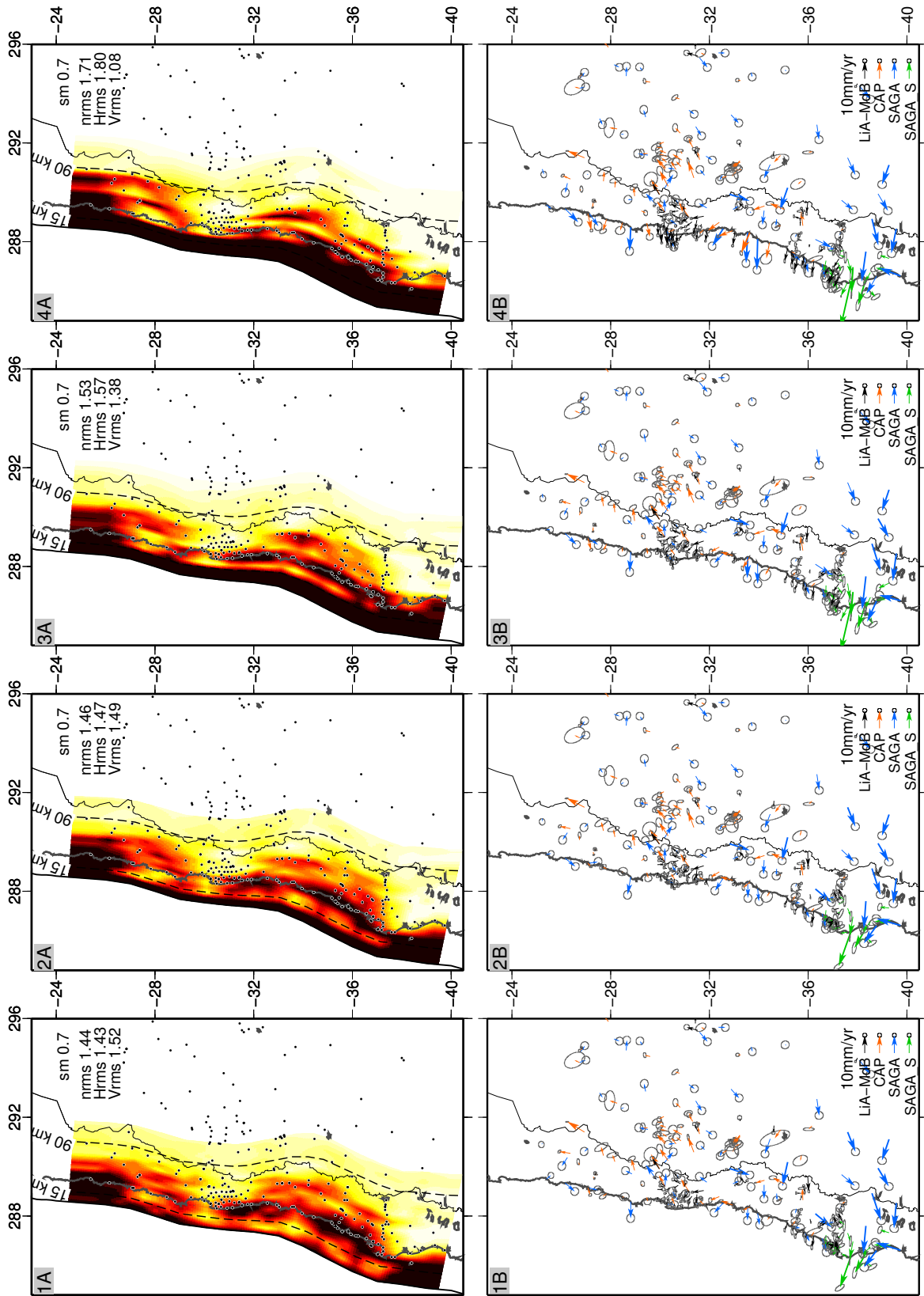


**Figure S3.** Coupling patterns inverted with imposed 100% coupling down to a variable depth (A row) and associated residuals (B row). Coupling is color coded as in Figure 5 and dashed curves are isodepth of the plunging slab. The roughness value, the whole root mean square (Nrms), the root mean square on horizontal data (Hrms) and on vertical data (Vrms) are indicated in the upper right corner of each coupling plot. Residuals are color coded as in Figure 3. Coupling is forced to 100% for the surface nodes (1A-1B), down to 7 km depth (2A-2B), down to 15 km depth (3A-3B) and down to 22.5 km (4A-4B).

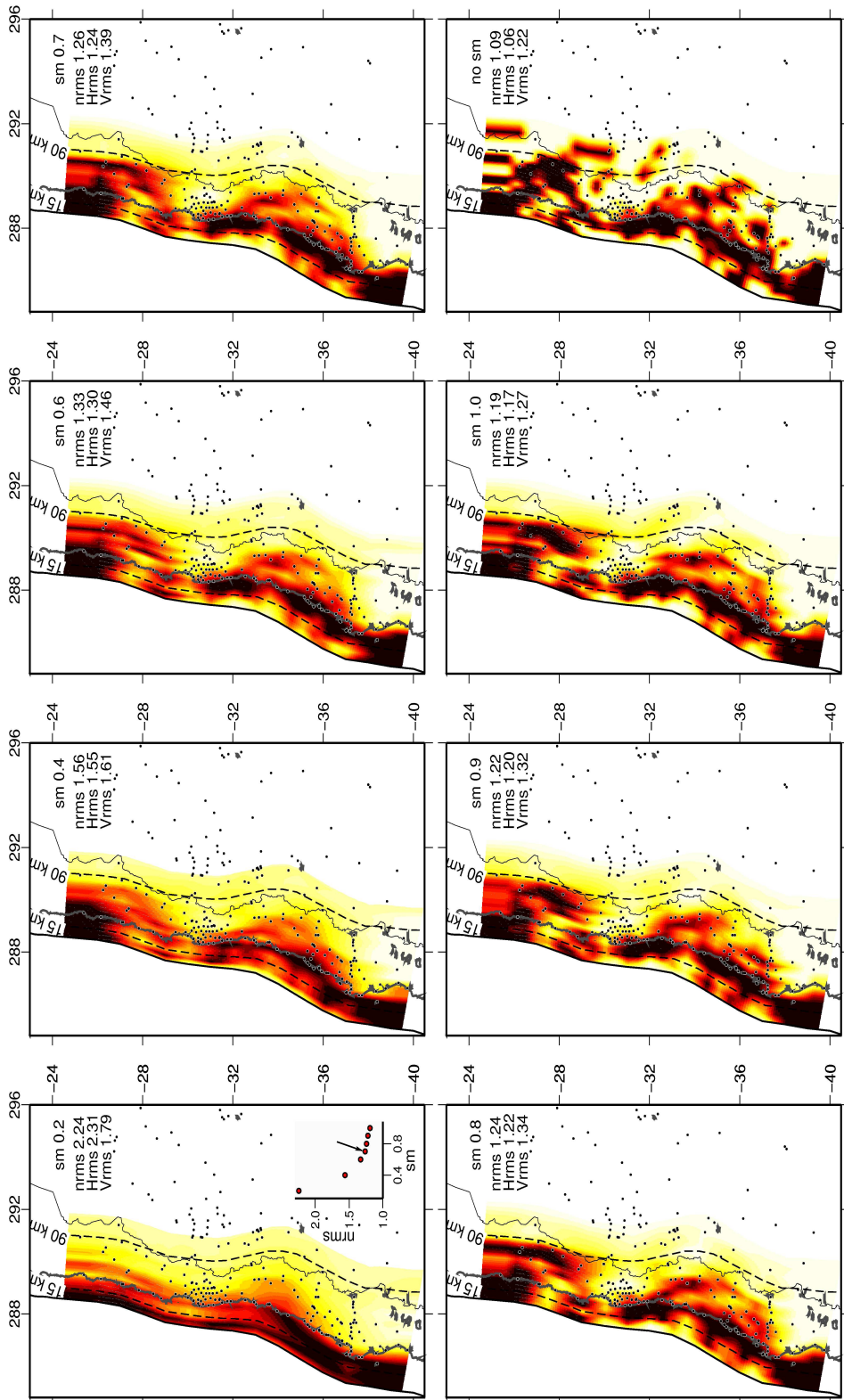


**Figure S4.** Coupling patterns inverted using different roughness values. Coupling is color coded as in Figure 5 and dashed curves are isodepth of the plunging slab. The roughness value, the whole root mean square (Nrms), the root mean square on horizontal data (Hrms) and on vertical data (Vrms) are indicated in the upper right corner of each plot. We plot the variations of Nrms with roughness in the bottom right corner of the smoothest inversion. The model with roughness coefficient 0.7 is the preferred model also shown in Figure 5.

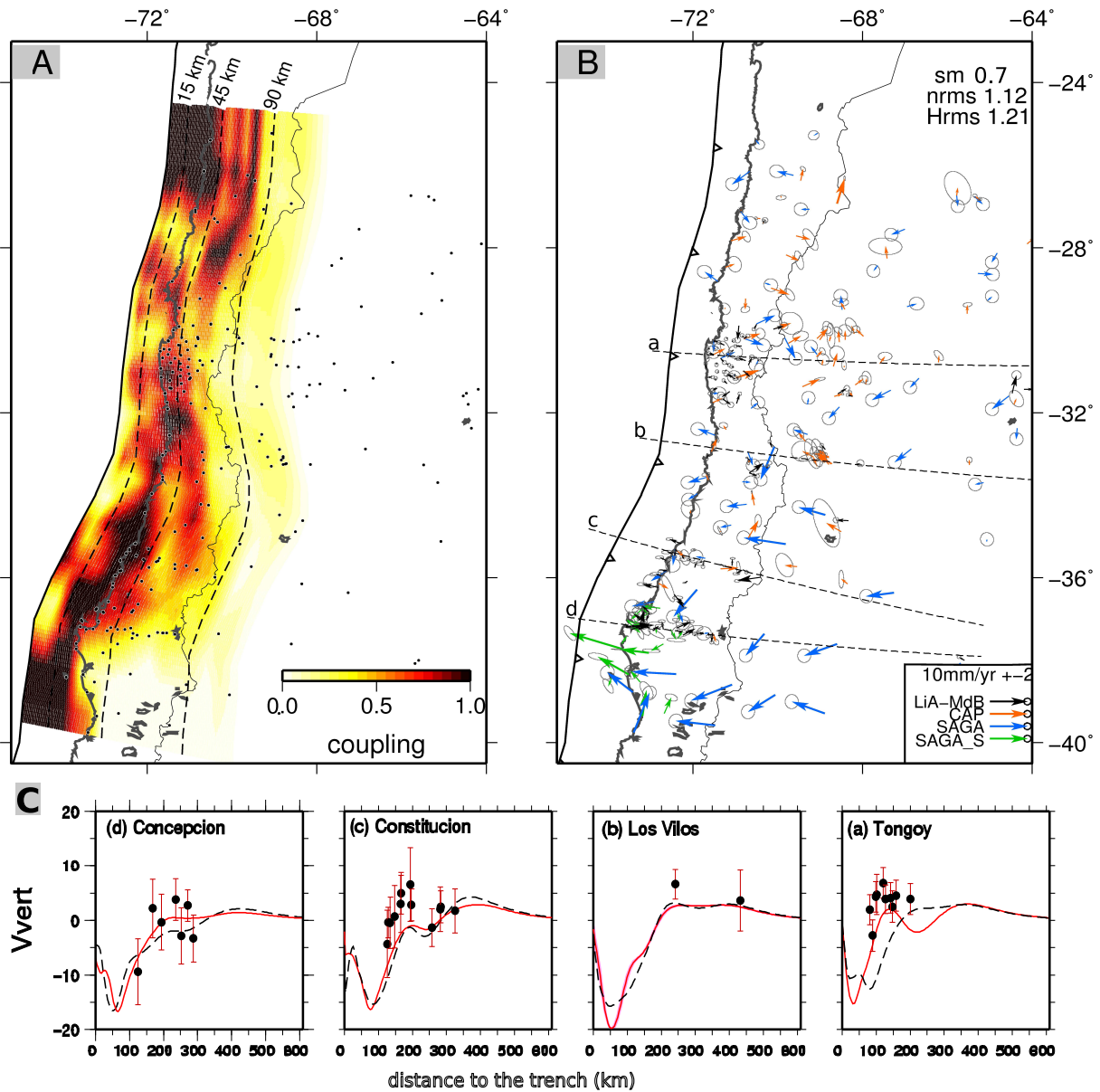


**Figure S5.** Coupling distribution obtained by the inversion of horizontal GPS data only (A) and associated residuals (B) with a smoothing coefficient of 0.7. The fit of this model to the vertical data set is plotted along four profile lines (dark dotted line in C) against with the surface deformation predicted by our “best-fit” model including the vertical data in the inversion (red plain line in C). Profil width is 20km.



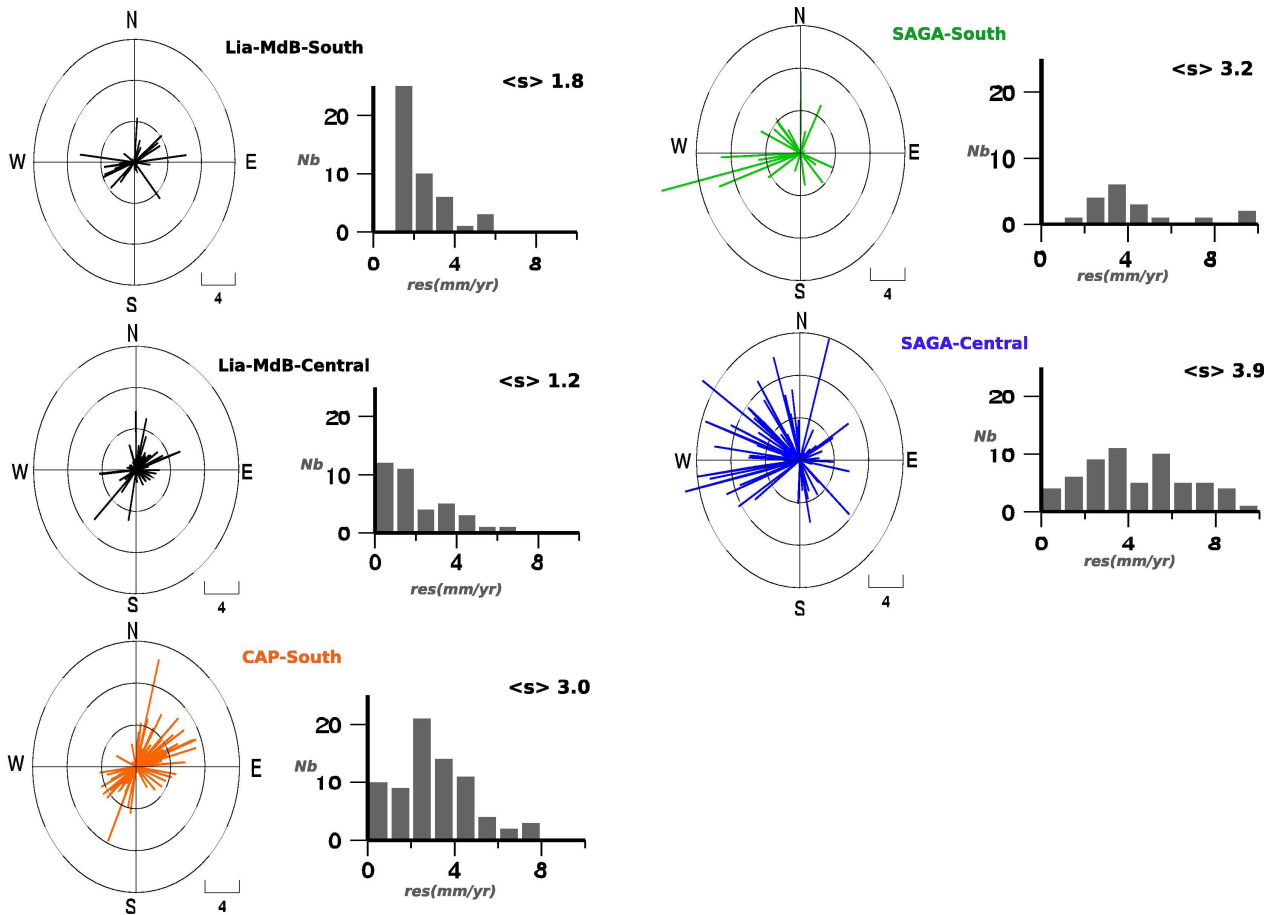


**Figure S6.** Detailed analysis of residuals. For each data-set, wind roses depict amplitude and orientation, histograms depict residuals distributions (scale is in mm/yr). The average uncertainty of each data-set after uncertainty rescaling is indicated by the  $\langle s \rangle$  value plotted in the upper right corner of the graphs. The largest residuals are obtained for the SAGA data-sets, either due to postseismic motion for the SAGA-south data-set (green), or to partial incompatibility with other data-sets.



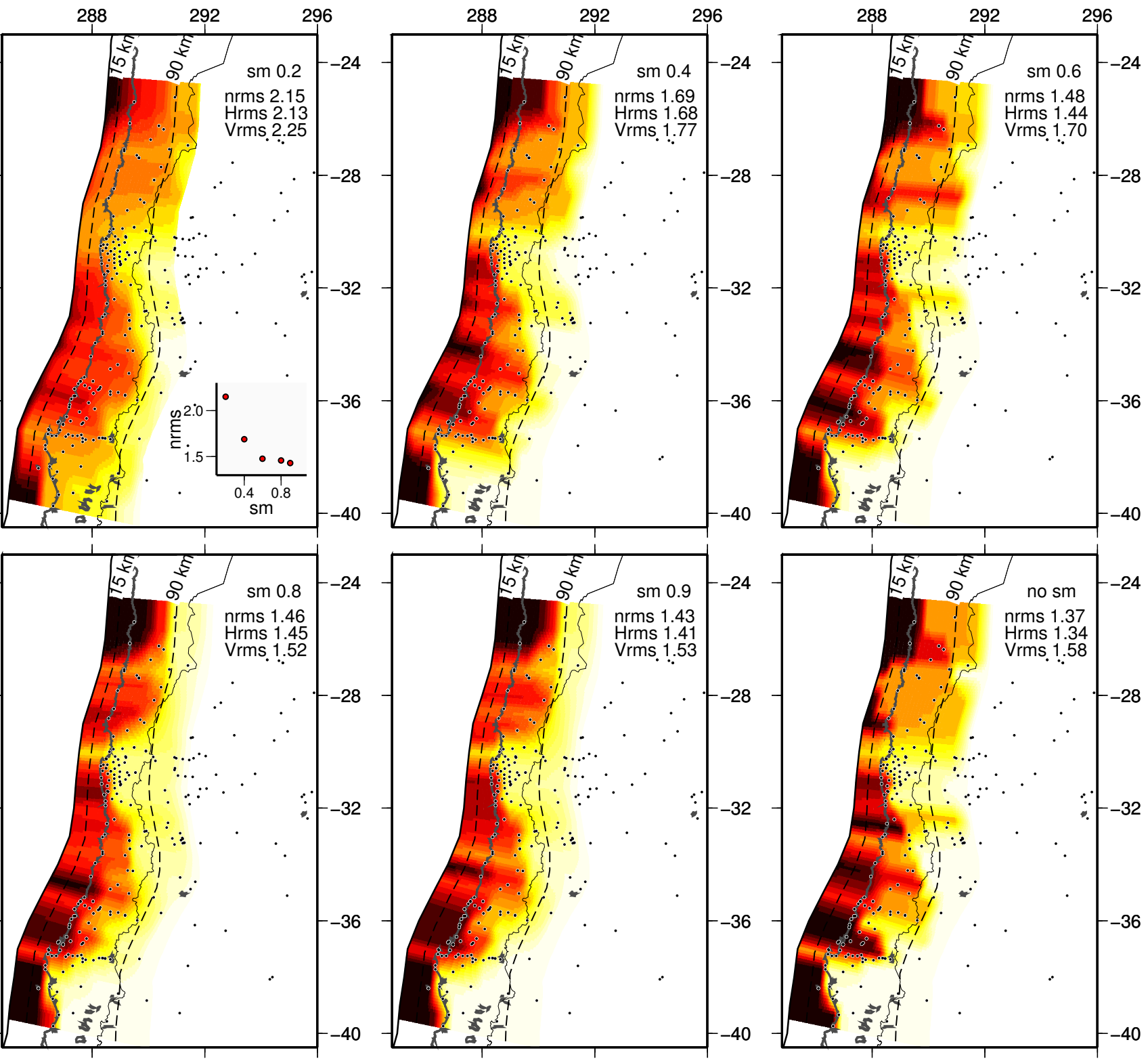


**Figure S7.** Same than Figure S4 but for inversions made with the down-dip decrease constrain on the coupling values.

Same than Figure S4 but for inversions made with the down-dip decrease constrain on the coupling values.